Observation of uncompensated bound charges at improper ferroelectric domain walls

Peggy Schoenherr,[†] Konstantin Shapovalov,[‡,¶] Jakob Schaab,[†] Zewu Yan,[§,‖] Edith D. Bourret,[‖] Mario Hentschel,[⊥] Massimiliano Stengel,[¶,#] Manfred Fiebig,[†] Andres Cano,[‡] and Dennis Meier[*,†,@]

†*Department of Materials, ETH Zürich, Vladimir-Prelog-Weg 4, 8093 Zurich, Switzerland*

‡*CNRS, Université de Bordeaux, ICMCB, UPR 9048, 33600 Pessac, France*

¶*Institut de Ciència de Materials de Barcelona (ICMAB-CSIC), Campus UAB, 08193 Bellaterra, Spain*

§*Department of Physics, ETH Zürich, Otto-Stern-Weg 1, 8093 Zurich, Switzerland*

‖*Materials Science Division, Lawrence Berkeley National Laboratory, California 94720, USA*

⊥*4th Physics Institute and Research Center SCoPE, University of Stuttgart, Pfaffenwaldring 57, 70569 Stuttgart, Germany*

#*ICREA—Institució Catalana de Recerca i Estudis Avançats, 08010 Barcelona, Spain*

@*Department of Materials Science and Engineering, Norwegian University of Science and Technology, NTNU, 7043 Trondheim, Norway*

E-mail: dennis.meier@ntnu.no,andres.cano@neel.cnrs.fr

Phone: +47 (0)735 94047

Note 1: Conductance and optical band gap

Conductive atomic force microscopy (cAFM) maps are recorded in forward bias (positive DC bias voltage applied to the tip) using an Pt-coated probe tip (ANSCM-Pt). The respective $I(V)$ curve is presented in Fig. S.1a, which is recorded at room temperature with the tip placed within a domain, i.e., away from the walls. The $I(V)$ data reflects the presence of a Schottky-like barrier between tip and sample as addressed in the main text.

In order to determine the optical band gap in $Er_{0.99}Ca_{0.01}MnO_3$ ($x = 0.01$), we performed temperature-dependent linear transmission spectroscopy measurements with light incident along the crystallographic surface normal. The measurements were conducted on a micro-spectrometer Jasco MSV-370[1] with a continuous flow micro-cryostat Janis SVT-500. Figure S.1b shows the linear spectroscopy data in the ultra-violet (620 nm $\sim$ 2 eV) to the near-infrared (2500 nm $\sim$ 0.5 eV) range (each temperature is separated by 15% for better visibility). Different absorption lines are observed between $0.80 - 0.85$ eV and around 1.28 eV, which can be assigned to $4f$ transitions of the Er^{3+} ions, corresponding to transitions between the ground state of the Er^{3+} ($^4I_{15/2}$) to $^4I_{13/2}$ and $^4I_{11/2}$.[2]

In addition, the spectra show the $d-d$ interband transition of the Mn^{3+} ions, which defines the band gap in hexagonal manganites.[3] The $d-d$ transition is visible as a step-like change in intensity, shifting to higher frequencies with decreasing temperature as indicated by the dotted line (Fig. S.1b). We find that the band gap varies from ≈ 1.4 eV at 300 K to ≈ 1.7 eV at 5 K, which is in agreement with previous measurements reporting a band gap of 1.6 eV for undoped $ErMnO_3$.[4]

The observed decrease in $d-d$ transition energy with increasing temperatures (shown in the inset to Fig. 1f in the main text) can be described based on the semi-empirical Varshni relation for semiconductors:[5]

$$E_{dd}(T) = E_{dd}(0) - \alpha T, \tag{S.1}$$

yielding $E_{dd}(0) = 1.68 \pm 0.02$ eV as the $d-d$ transition energy at 0 K, and $\alpha = 0.92 \pm$

0.09 meV/K as material-dependent constant.

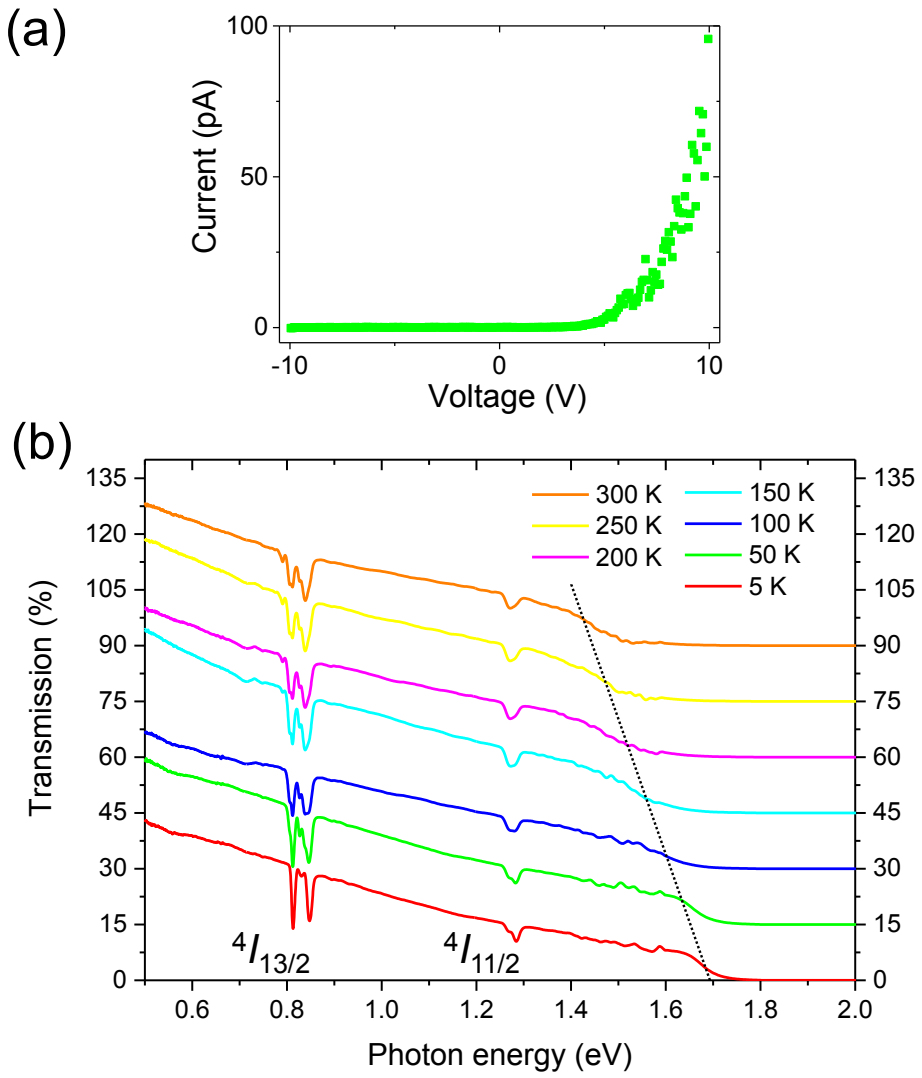

Figure S.1: (a) $I(V)$ characteristic of $Er_{0.99}Ca_{0.01}MnO_3$ ($x = 0.01$) at room temperature. (b) Linear transmission spectroscopy measurements from the ultra-violet (620 nm $\sim$ 2 eV) to the near-infrared (2500 nm $\sim$ 0.5 eV) for a 44 μm thick $Er_{0.99}Ca_{0.01}MnO_3$ sample. Transmission spectra for temperatures between 300 K and 5 K. Spectra are offset by 15% with respect to each other for better visibility.

Note 2: Topography

Figure S.2 show the topographic images taken at room temperature of Fig. 1 and Fig. 2 of the main text. Both images have a roughness below 0.3 nm with an almost uniformly flat

surface. This shows that the topography will not give additional contributions to the EFM signal at lower temperatures.

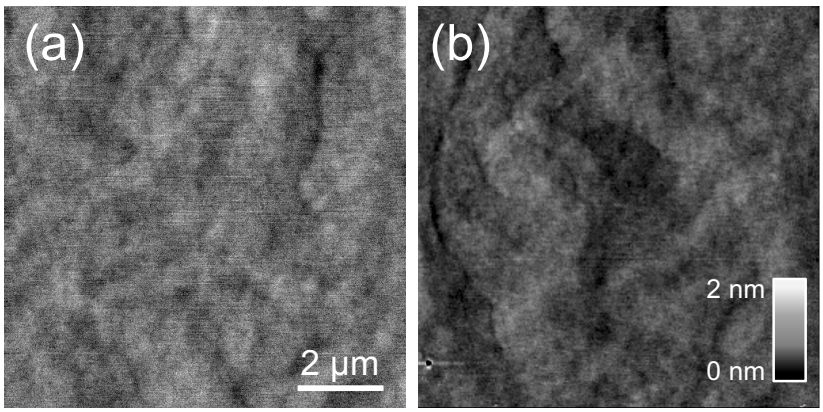

Figure S.2: Topography images in (a) and (b) corresponding AFM measurements in Fig. 1 and Fig. 2 of the main text, respectively.

Note 3: Numerical modeling of the EFM response

In order to simulate the temperature evolution of the EFM response shown in Fig. 3 of the manuscript, we developed a numerical model implementing the finite-element method. The modeling is done in two steps.

First, we calculate the band structure (Fig. 4(a) of the main text) and the distribution of charges around the domain walls in a p-type semiconductor, assuming electrostatic equilibrium in the sample, that is, full screening of charges. This scenario corresponds to the domain-wall high-temperature regime with $T > T^*$. We consider a pair of tail-to-tail and head-to-head domain walls, separated by $L = 500$ nm, which corresponds to a realistic distance as seen from the cAFM and EFM images in Fig. 2. The equations governing the

variations of the potential $\phi(x)$ around the walls are:

$$-\epsilon\frac{d^2\phi}{dx^2} = en_h(\phi,T) - en_e(\phi,T) - eN_A^-(\phi,T) + \rho_b, \tag{S.2}$$

$$n_h(\phi,T) = N_V(T)F_{1/2}\left(-\frac{E_F+e\phi}{kT}\right), \tag{S.3}$$

$$n_e(\phi,T) = N_C(T)F_{1/2}\left(-\frac{E_g-E_F-e\phi}{kT}\right), \tag{S.4}$$

$$N_A^-(\phi,T) = N_A/\left(1+4\exp\left[\frac{\Delta_A-E_F-e\phi}{kT}\right]\right), \tag{S.5}$$

$$\rho_b = \frac{P_S}{\xi_6}\left(-\frac{1}{\cosh^2[(x+L/2)/\xi_6]}+\frac{1}{\cosh^2[(x-L/2)/\xi_6]}\right), \tag{S.6}$$

where $n_h(\phi,T)$ and $n_e(\phi,T)$ are the hole and electron densities, $N_A^-(\phi,T)$ is the density of the ionized acceptors, Δ_A is the acceptor energy level above the valence band maximum, ρ_b is the bound charge at the tail-to-tail ($x=-L/2$) and head-to-head ($x=L/2$) walls, $F_{1/2}(z) = (2/\sqrt{\pi})\int_0^\infty t^{1/2}dt/(1+\exp(t-z))$ is the complete Fermi-Dirac integral, $\xi_6 \sim 0.5$ nm is the correlation length determining the width of the domain wall[6] and $P_S = 7.1\ \mu\mathrm{Ccm}^{-2}$ is the polarization at room temperature.[7] In our calculations, non-degenerate and degenerate regimes are both taken into account by considering the complete Fermi-Dirac integral in Eqs. (S.3–S.4), which is implemented as

$$F_{1/2}(z) \approx \exp(z), \qquad z < -4 \text{ (non-degenerate regime)} \tag{S.7}$$

$$F_{1/2}(z) \approx \frac{4}{3\sqrt{\pi}}z^{3/2}, \qquad z > 4 \text{ (degenerate regime)} \tag{S.8}$$

$$F_{1/2}(z) \approx \exp\left(\sum_{i=0}^{3} a_i z^i\right), \qquad -4 < z < 4 \text{ (interpolation in between)} \tag{S.9}$$

in our calculations. After numerically solving Eq. (S.2), using the material constants given in the main text along with $N_V(T) = N_C(T) = 2.415\times10^{15}\ (\mathrm{cm}^{-3}\mathrm{K}^{-3/2})\cdot T^{3/2}$, we obtain the band structure as shown in Fig. 4(a) of the main text for $N_A = 2\times10^{18}\ \mathrm{cm}^{-3}$. The band diagram is in agreement with previous analytical and DFT-based calculations,[8,9] showing that the tail-to-tail domain wall is screened by mobile holes within the wall, and that the

head-to-head wall is screened partially by the inversion electron layer within the domain wall as well as a hole depletion layer of the width $2w = \sqrt{8\epsilon E_g/e^2 N_A}$. The charge screened by the hole depletion layer is $2weN_A$.

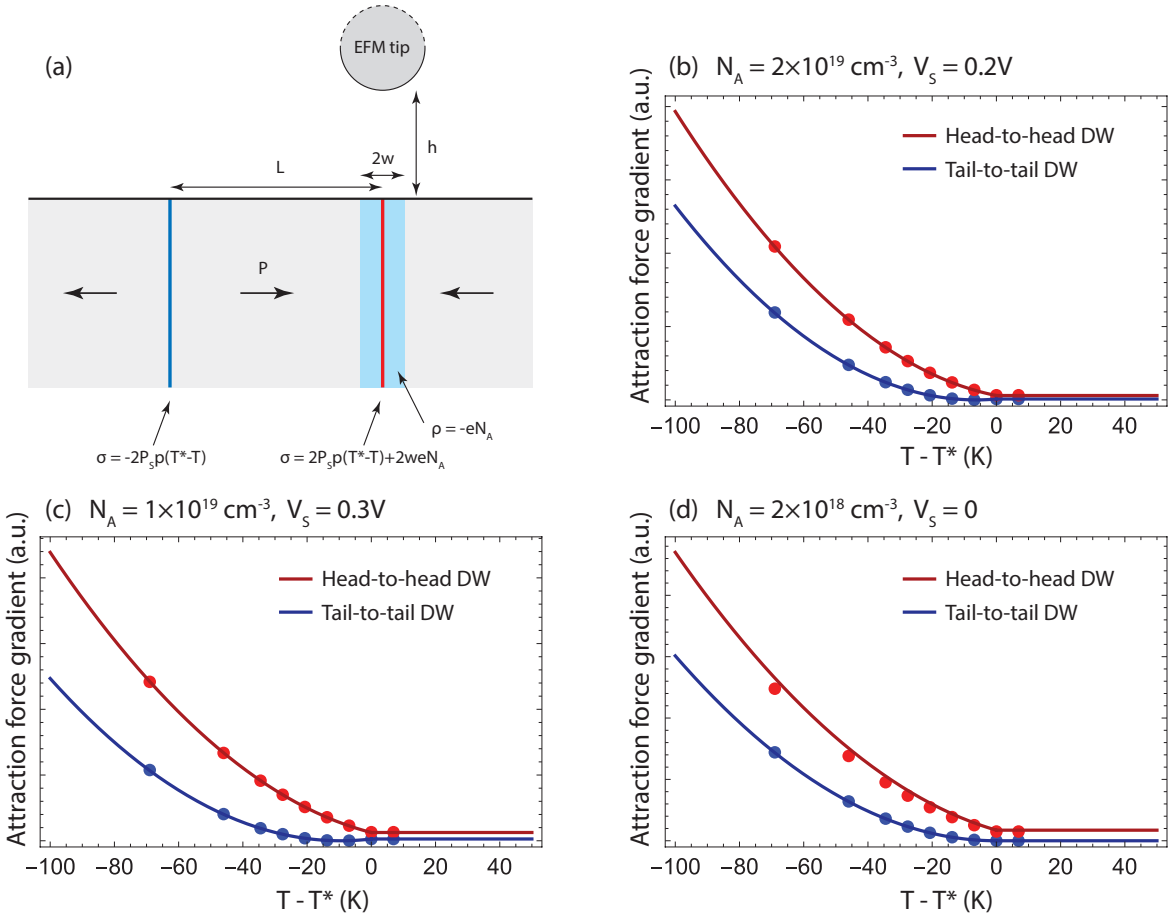

Figure S.3: (a) Schematics of the 2D numerical model, with sheet charge densities σ at the domain walls (dark-blue and red lines) and volume charge density ρ in the hole-depletion layer (light-blue area). (b-d) Results of numerical calculations of the attraction force gradient (dots), fitted with ∇F_{TT} and ∇F_{HH} (solid lines, see Eq. (S.14)).

Using the information about the charge distribution obtained from the first step, we develop a 2D model for the material in the low-temperature insulating regime ($T < T^*$). We consider a 200 nm thick dielectric slab (representing $Er_{1-x}Ca_xMnO_3$) with charges derived from the calculated band diagram as well as additional uncompensated pyroelectric bound charges that arise at lower temperatures (Fig. S.3(a)). The pyroelectric constant is taken as

$p = 1.5$ nC/cm^2·K, lying between the experimentally extracted value for $HoMnO_3$ at 100 K (0.6 nC/cm^2·K)[10] and the theoretical value for $YMnO_3$ (3 nC/cm^2·K) obtained using the theory of Ref. 11.

We place a circular-shaped metallic EFM tip at distance $h \sim 30$ nm from the sample surface above the head-to-head or the tail-to-tail wall (see Fig. S.3(a)), and calculate the electrostatic potential distribution $\phi(x, y)$ ($\mathbf{y}$ is perpendicular to the surface). The force $\mathbf{F}(h)$ of the electrostatic attraction of the tip to the dielectric slab is

$$\mathbf{F}(h) = \oint_{\text{tip@}h} \frac{\epsilon_0 (\nabla\phi)^2}{2} d\mathbf{S}. \tag{S.10}$$

The force gradient acting as the EFM contrast is calculated as $d\mathrm{F}_y/dh \approx [F_y(30\text{ nm}) - F_y(29\text{ nm})]/1$ nm.

The evolution of the resulting force gradient with temperature is obtained for several acceptor densities and surface potentials. For $N_A = 2 \times 10^{18}$ cm^{-3}, the calculations are performed for a grounded tip ($V_S = 0$). For $N_A = 1 \times 10^{19}$ cm^{-3} and $N_A = 2 \times 10^{19}$ cm^{-3}, we perform calculations with different voltages at the tip simulating a surface potential (a surface potential induces mirror charges on the tip), ranging from $V_S = 0$ V to $V_S = -0.3$ V. All calculations are done at eight different temperatures, with $T^* - T$ ranging from 0 K to 70 K.

The calculated data points are then fitted to analytical curves. In order to do it, we first separately consider the scaling behavior of $F(h, N_A, T, V_S)$ for each of the three main mechanisms of attraction described in the manuscript: F_{deplet} is the force from the depletion layer surrounding the head-to-head walls; F_{uncomp} accounts for the uncompensated pyroelectric bound charges at the wall at $T < T^*$; and F_{surf} results from the sample surface due to the surface potential V_S. First of all, we note that the electric field generated by the uncompensated charges is proportional to $(T^* - T)$, and so $F_{\text{uncomp}} \propto (T^* - T)^2$; likewise, $F_{\text{surf}} \propto V_S^2$. The electric field generated by the depletion layer can be estimated by setting $\epsilon = \epsilon_0$ inside

the sample, and calculating the electric potential from the quadrupole-like distribution of charges surrounding the wall:

$$\phi(x,y) = \int_{-\infty}^{0} dy_0 \left(2weN_A\phi_\lambda(x, y-y_0) - eN_A \int_{-w}^{w} dx_0 \phi_\lambda(x-x_0, y-y_0) \right) \approx \frac{eN_A}{6\pi\epsilon_0}\frac{w^3}{y} \propto \frac{1}{\sqrt{N_A}y}, \tag{S.11}$$

where $\phi_\lambda = \log(x^2+y^2)/2\pi\epsilon_0$ is the potential from a unit line charge. Thus, the electric field

$$E_{\text{deplet}} = -\frac{\partial\phi}{\partial y} \propto \frac{1}{\sqrt{N_A}y^2}, \tag{S.12}$$

and $F_{\text{deplet}} \propto N_A^{-1}$.

The scaling $F(h)$ of each of the three forces is extracted by performing another set of finite-elements simulations at varying distances h of the tip from the film surface. We obtain:

$$F_{\text{uncomp}} \propto (T^* - T)^2 h^{-1.56}, \quad F_{\text{deplet}} \propto N_A^{-1} h^{-2.94}, \quad F_{\text{surf}} \propto V_S^2 h^{-1.48}. \tag{S.13}$$

Note that $F_{\text{deplet}} \propto h^{-2.94}$ in Eq. (S.13) is different from $F_{\text{deplet}} \propto E^2 \propto h^{-4}$ estimated in Eq. (S.12) – this difference is due to the large dielectric constant of the material ($\epsilon = 13\epsilon_0$) and the distortions of the electric field around the metallic EFM tip, not taken into account for the estimate.

Combining the expressions in Eq. (S.13) together, we obtain the analytical fitting curves for the force gradients ∇F_{TT} at the tail-to-tail and ∇F_{HH} at the head-to-head walls:

$$\nabla F_{\text{TT}} = \frac{\epsilon_0}{2}\frac{dE_{\text{TT}}^2}{dh}, \qquad \nabla F_{\text{HH}} = \frac{\epsilon_0}{2}\frac{dE_{\text{HH}}^2}{dh}, \tag{S.14}$$

$$E_{\text{TT}} = -C_{\text{uncomp}}(T^* - T)h^{-0.78} + C_{\text{surf}}V_S h^{-0.74}, \tag{S.15}$$

$$E_{\text{HH}} = C_{\text{uncomp}}(T^* - T)h^{-0.78} + C_{\text{deplet}}N_A^{-1/2}h^{-1.47} + C_{\text{surf}}V_S h^{-0.74}, \tag{S.16}$$

where E_{TT} and E_{HH} are effective electric fields from tail-to-tail and head-to-head walls acting

on the EFM tip. Constants C_{uncomp}, C_{deplet} and C_{surf} are extracted from our numerical simulations by fitting Eq. (S.14) to four data points: gradients of the attraction force at head-to-head and tail-to-tail domain walls calculated at two different surface potentials $V_S = 0.3$ V and $V_S = 0$ V, with $N_A = 2{\times}10^{19}$ cm^{-3}, $T^* - T = 70$ K. With the three C constants extracted, Eqs. (S.14–S.16) give the analytic approximation of the force gradients at both domain walls at a wide range of parameters (N_A, V_S, T), reproducing the results of our numerical simulations with a remarkably good accuracy – see Fig. S.3(b-d) for some examples.

References

(1) Dombrowski, D. Linear optische Spektroskopie and dünnen Schichten und Multiferroika. Bachelor thesis, University of Bonn, 2011.

(2) Dieke, G. H. *Spectra and Energy Levels of Rare Earth Ions in Crystals*; John Wiley & Sons: New York, London, Sydney, Toronto, 1968.

(3) Degenhardt, C.; Fiebig, M.; Fröhlich, D.; Lottermoser, T.; Pisarev, R. Nonlinear optical spectroscopy of electronic transitions in hexagonal manganites. *Applied Physics B* **2001**, *73*, 139–144.

(4) Kalashnikova, A. M.; Pisarev, R. V. Electronic structure of hexagonal rare-earth manganites $R\mathrm{MnO_3}$. *JETP Letters* **2003**, *78*, 143–147.

(5) Varshni, Y. Temperature dependence of the energy gap in semiconductors. *Physica* **1967**, *34*, 149–154.

(6) Holtz, M. E.; Shapovalov, K.; Mundy, J. A.; Chang, C. S.; Yan, Z.; Bourret, E.; Muller, D. A.; Meier, D.; Cano, A. Topological Defects in Hexagonal Manganites: Inner Structure and Emergent Electrostatics. *Nano Letters* **2017**, *17*, 5883–5890.

(7) Stengel, M.; Fennie, C. J.; Ghosez, P. Electrical properties of improper ferroelectrics from first principles. *Physical Review B* **2012**, *86*, 094112.

(8) Eliseev, E. A.; Morozovska, A. N.; Svechnikov, G. S.; Gopalan, V.; Shur, V. Y. Static conductivity of charged domain walls in uniaxial ferroelectric semiconductors. *Physical Review B* **2011**, *83*, 1–8.

(9) Mundy, J. A. et al. Functional electronic inversion layers at ferroelectric domain walls. *Nature Materials* **2017**, *16*, 622–627.

(10) Hur, N.; Jeong, I. K.; Hundley, M. F.; Kim, S. B.; Cheong, S.-W. Giant magnetoelectric effect in multiferroic $HoMnO_3$ with a high ferroelectric transition temperature. *Physical Review B* **2009**, *79*, 134120.

(11) Artyukhin, S.; Delaney, K. T.; Spaldin, N. A.; Mostovoy, M. Landau theory of topological defects in multiferroic hexagonal manganites. *Nature Materials* **2014**, *13*, 42–49.